MICROROBOTS

Imaging-guided bioresorbable acoustic hydrogel microrobots

Hong Han[1]†, Xiaotian Ma[1]†, Weiting Deng[1,2]†, Junhang Zhang[3]†, Songsong Tang[1], On Shun Pak[4], Lailai Zhu[5], Ernesto Criado-Hidalgo[1,6], Chen Gong[3], Emil Karshalev[1], Jounghyun Yoo[1], Ming You[1], Ann Liu[6], Canran Wang[1], Hao K. Shen[6], Payal N. Patel[1], Claire L. Hays[1], Peter J. Gunnarson[7,8], Lei Li[1], Yang Zhang[1], John O. Dabiri[7,8], Lihong V. Wang[1], Mikhail G. Shapiro[1,6,9], Di Wu[6]*, Qifa Zhou[3]*, Julia R. Greer[1,2]*, Wei Gao[1]*

Micro- and nanorobots excel in navigating the intricate and often inaccessible areas of the human body, offering immense potential for applications such as disease diagnosis, precision drug delivery, detoxification, and minimally invasive surgery. Despite their promise, practical deployment faces hurdles, including achieving stable propulsion in complex in vivo biological environments, real-time imaging and localization through deep tissue, and precise remote control for targeted therapy and ensuring high therapeutic efficacy. To overcome these obstacles, we introduce a hydrogel-based, imaging-guided, bioresorbable acoustic microrobot (BAM) designed to navigate the human body with high stability. Constructed using two-photon polymerization, a BAM comprises magnetic nanoparticles and therapeutic agents integrated into its hydrogel matrix for precision control and drug delivery. The microrobot features an optimized surface chemistry with a hydrophobic inner layer to substantially enhance microbubble retention in biofluids with multiday functionality and a hydrophilic outer layer to minimize aggregation and promote timely degradation. The dual-opening bubble-trapping cavity design enables a BAM to maintain consistent and efficient acoustic propulsion across a range of biological fluids. Under focused ultrasound stimulation, the entrapped microbubbles oscillate and enhance the contrast for real-time ultrasound imaging, facilitating precise tracking and control of BAM movement through wireless magnetic navigation. Moreover, the hydrolysis-driven biodegradability of BAMs ensures its safe dissolution after treatment, posing no risk of long-term residual harm. Thorough in vitro and in vivo experimental evidence demonstrates the promising capabilities of BAMs in biomedical applications. This approach shows promise for advancing minimally invasive medical interventions and targeted therapeutic delivery.

INTRODUCTION

The emergence of micro- and nanorobotics heralds a pivotal shift in biomedical engineering, introducing a new era filled with unparalleled prospects to refine a myriad of applications including disease diagnosis, targeted drug delivery, detoxification, and minimally invasive surgery (*1*–*12*). These miniature devices, adept at traversing the complex and often unreachable recesses of the human body, stand at the forefront of precision medicine. The diverse propulsion mechanisms used by these microrobots, which include the deployment of local chemical fuels or external fields, such as a magnetic field, an ultrasound field, or light, or the exploitation of natural microorganisms' motility, illustrate the approaches engineered to navigate these devices across micro- and nanoscale environments (*13*–*18*). However, the practical application of these advancements in vivo is impeded by challenges in the propulsion through complex biofluids, real-time imaging, precise control, and therapeutic assessment of micromotors (*19*–*24*).

For an untethered microrobot to operate effectively in the complex biological milieu of the human body, it must encompass a suite of characteristics: reliable and steady propulsion through biological media, enhanced imaging contrast for real-time visualization under deep tissue, meticulous control for accurate targeting of diseased regions, substantial payload capacity for effective therapy, and high biocompatibility with biodegradable characteristics to obviate the need for surgical removal. Moreover, high-resolution additive manufacturing and high-freedom design are critical for the widespread clinical adoption of microrobots. Nonetheless, an intricate challenge lies in integrating these optimal features within the confines of a micro- or nanoscale robotic platform, given the inherent limitations posed by their diminutive size.

Among the emerging solutions, acoustically actuated microrobots show great promise owing to the distinct advantages of acoustic propulsion, including safety, noninvasive operation, deep-tissue penetration, robust propulsive forces, rapid response, and untethered control, which are well aligned with clinical demands (*25*–*38*). In particular, microrobots that incorporate bubbles and leverage microbubble oscillations induced by weak traveling acoustic waves offer an attractive approach to in vivo manipulation (*39*–*42*). However, the practical deployment of these microrobots faces obstacles because of the transient stability and short life span of the encapsulated bubble within biological fluids and the lack of precisely controlled propulsion in complex environments in vivo (*43*, *44*).

[1]Andrew and Peggy Cherng Department of Medical Engineering, Division of Engineering and Applied Science, California Institute of Technology, Pasadena, CA, USA. [2]Kavli Nanoscience Institute, California Institute of Technology, Pasadena, CA, USA. [3]Alfred E. Mann Department of Biomedical Engineering, University of Southern California, Los Angeles, CA, USA. [4]Department of Mechanical Engineering, Santa Clara University, Santa Clara, CA, USA. [5]Department of Mechanical Engineering, National University of Singapore, Singapore, Singapore. [6]Division of Chemistry and Chemical Engineering, California Institute of Technology, Pasadena, CA, USA. [7]Graduate Aerospace Laboratories, California Institute of Technology, Pasadena, CA, USA. [8]Department of Mechanical and Civil Engineering, California Institute of Technology, Pasadena, CA, USA. [9]Howard Hughes Medical Institute, Pasadena, CA, USA.
*Corresponding author. Email: weigao@caltech.edu (W.G.); jrgreer@caltech.edu (J.R.G.); qifazhou@usc.edu (Q.Z.); dwwu@caltech.edu (D.W.)
†These authors contributed equally to this work.

In response to these multifaceted challenges, we introduce a hydrogel-based, imaging-guided, bioresorbable acoustic microrobot (BAM) designed for navigation with high stability, precision, and control within the human body (Fig. 1A and Movie 1). The fabrication of BAMs involves two-photon polymerization (TPP), using a composite material consisting of poly(ethylene glycol) diacrylate (PEGDA); pentaerythritol tetraacrylate (PETA); and additional functional components including Fe_3O_4 nanoparticles (NPs) for magnetic steering and therapeutic agents such as the anticancer drug 5-fluorouracil (5-FU) (Fig. 1, A to C). A BAM's refined design incorporates an asymmetric dual-opening bubble-trapping cavity, substantially elevating its propulsion capabilities beyond the single-opening configuration (Fig. 1, C and D, and fig. S1). A unique dual-step surface chemistry modification strategy endows BAMs with a hydrophobic inner surface, substantially improving bubble retention within biofluids, and a hydrophilic outer surface that prevents microrobot aggregation and promotes hydrogel degradation (Fig. 1E). These BAMs are capable of sustained, efficient acoustic propulsion in a variety of biological fluids—including urine, gastrointestinal fluid, and whole blood—over multiday durations (Fig. 1F).

In addition to their attractive propulsion abilities, the microbubbles trapped by BAMs serve as effective ultrasound imaging contrast agents (*45*, *46*). Thus, the movement and localization of BAMs can be monitored in real time with high spatiotemporal resolution using

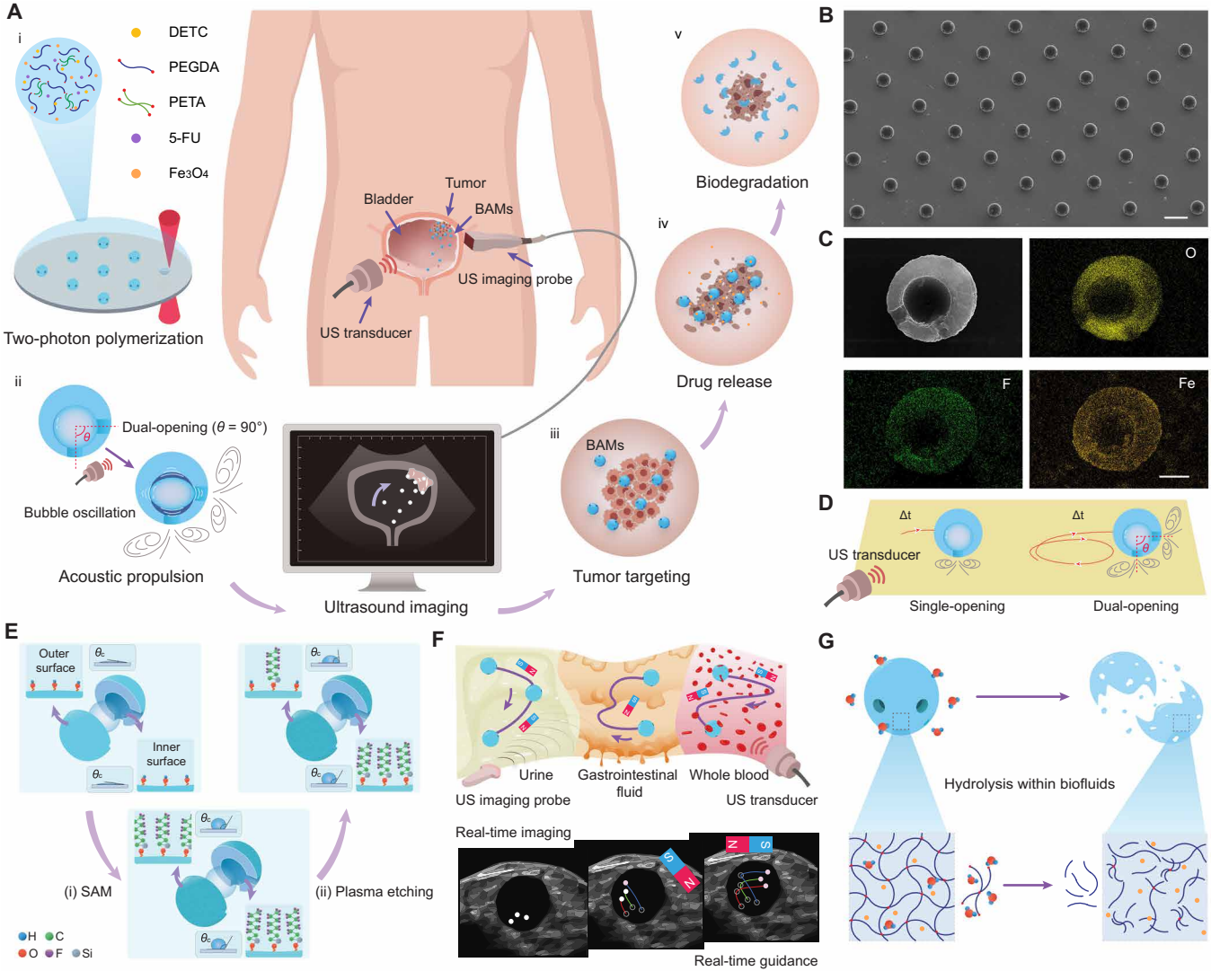

Fig. 1. Imaging-guided BAMs. (**A**) Schematic illustration of the preparation and in vivo applications of BAMs, covering the fabrication of BAMs by TPP with a customized polymer resin (i), the efficient propulsion of the dual-opening BAM configuration (ii), ultrasound imaging-guided BAMs for targeted drug delivery (iii), sustainable drug release at the diseased area from BAMs (iv), and biodegradation of the BAM backbone in vivo over time (v). US, ultrasound. (**B**) SEM images of a 3D-printed BAM array. Scale bar, 50 μm. (**C**) SEM image of a single BAM and the corresponding energy-dispersive x-ray spectroscopy mapping of O, F, and Fe elements, respectively. Scale bar, 10 μm. (**D**) Schematic illustration of the substantially enhanced propulsion behavior of dual-opening BAMs compared with single-opening BAMs. θ, the angle of the two openings. (**E**) Schematic illustration of the dual-step surface chemistry strategy used by the BAMs to preserve microbubbles for extended periods of operation in biologically relevant environments. θ_c, surface contact angle. (**F**) Schematic illustration of the efficient acoustic propulsion, ultrasound imaging, and magnetic control of BAMs in different biofluids in vivo. (**G**) Schematic of the hydrolysis-based biodegradation of BAMs in biofluids.

an ultrasound probe under deep tissue and directed with precision via wireless magnetic navigation (Fig. 1F). The harmonious combination of advanced and stable ultrasound-driven propulsion with concurrent imaging capabilities emphasizes the considerable potential of BAMs for in vivo biomedical applications. Last, the hydrolysis-mediated biodegradability of the BAM design ensures safe biological compatibility, devoid of harmful residue risks after operation (Fig. 1G). BAMs' performance, functionality, and efficacy for cancer therapy have been evaluated through extensive in vitro and in vivo experimental validations.

RESULTS

The design and motion characterization of BAMs

The hydrogel-based BAMs, fabricated via high-resolution TPP, feature a spherical design with an outer diameter of 30 μm and a spherical 18-μm-diameter internal cavity designed to trap microbubbles in aqueous environments (Fig. 1, B and C). Under an ultrasound field, the encapsulated gas bubbles within BAMs pulsate, oscillating at their resonant frequency, which could be tuned by the size of the internal cavity (table S1). This oscillation of the gas-liquid interface produces powerful microstreaming vortices around the openings (Fig. 1D), generating a propulsive force (F_p) in the opposite direction of the flow.

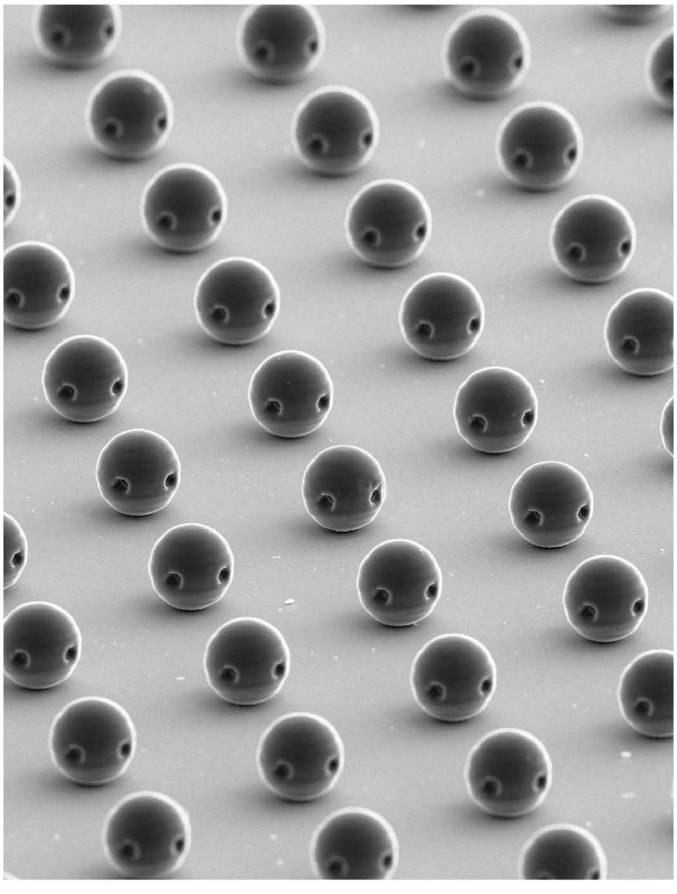

Movie 1. Overview of the imaging-guided bioresorbable acoustic hydrogel microrobots.

A notable aspect of BAM movement is the influence of secondary Bjerknes force (F_{SB}), an attractive force that acts perpendicular to the boundary (*47*, *48*). For microrobots with a single opening, the combined forces orient the opening toward the boundary and lead to unstable and inefficient translational movement (Fig. 2A). In contrast, BAMs designed with dual openings benefit from an additional propulsive force that runs parallel to the boundary, notably improving both speed and stability of movement (Fig. 2, B to D; fig. S2; and movie S1). An asymmetric design, in which the geometric center of the entrapped bubble deviates from the geometric center of BAM, was observed to exhibit enhanced propulsion performance (fig. S3A). This effect may be attributed to the closer proximity of the liquid-gas interfaces to the openings in the off-centered design, which generates more pronounced streaming flows (movie S2) and, thus, improves propulsion. As a result, asymmetric BAMs achieve propulsion speeds exceeding twice those of the symmetric design (fig. S3B).

Our experiments revealed the crucial role of the angle between the BAMs' openings (θ) in determining their performance. Specifically, the average speed of BAMs in phosphate-buffered saline (PBS) varied with θ, reaching a peak at 90° before decreasing. Speed measurements at 0°, 60°, 90°, 120°, and 150° were 413 ± 69, 1251 ± 188, 2043 ± 280, 754 ± 166, and 500 ± 47 μm s^{-1}, respectively. Given that one of the openings will face the substrate, the optimal speed at θ = 90° is attributed to the propulsive force generated from the second opening being absent of a *y*-direction component; thus, F_{p2} for θ = 90° contributed all to motion when comparing that with the other angles (θ = 60°, 90°, 120°, and 150°; fig. S4), as corroborated by simulations indicating the maximum streaming force at this angle (Fig. 2D and Supplementary Methods). When moving close to the wall, BAMs could be attracted to the wall because of the secondary Bjerknes force and move along the wall (fig. S5 and movie S3).

The microstreaming patterns generated by single-opening and dual-opening BAMs under the same ultrasound field were experimentally characterized with the passive particle tracers around the BAMs anchored on the substrate (Fig. 2, E and F; fig. S6; and movie S4). Particle image velocimetry (PIV) analysis revealed pronounced microstreaming patterns from both openings in the dual-opening configuration (Fig. 2, E and F). This further indicates the capability of generating propulsive thrust in additional directions compared with the single-opening design, as validated by both experimental data and simulation outcomes (Fig. 2, E to H; fig. S6; and Supplementary Methods). Several triple-opening BAMs were further investigated but displayed slower speeds than the dual-opening ones. This might be due to the partial cancellation of propulsion forces in the triple-opening structures (fig. S7). These findings underline the effectiveness of the dual-opening architecture in enhancing the propulsion and maneuverability of BAMs in fluidic environments.

Surface modification of BAMs for enhanced operation longevity in biofluids

The performance of BAMs in vivo relies on their ability to sustain microbubbles, which is crucial for both propulsion and imaging. The short life span of microbubbles in existing bubble-based microrobots has limited their practical use in biomedical applications. Previous reports have used surface engineering and structural design to prolong bubble retention (*39*, *41*, *49*). However, the use of bioresorbable materials in BAMs presents additional hurdles, particularly because of the hydrophilic nature of hydrogel surfaces, which complicates prolonged bubble retention.

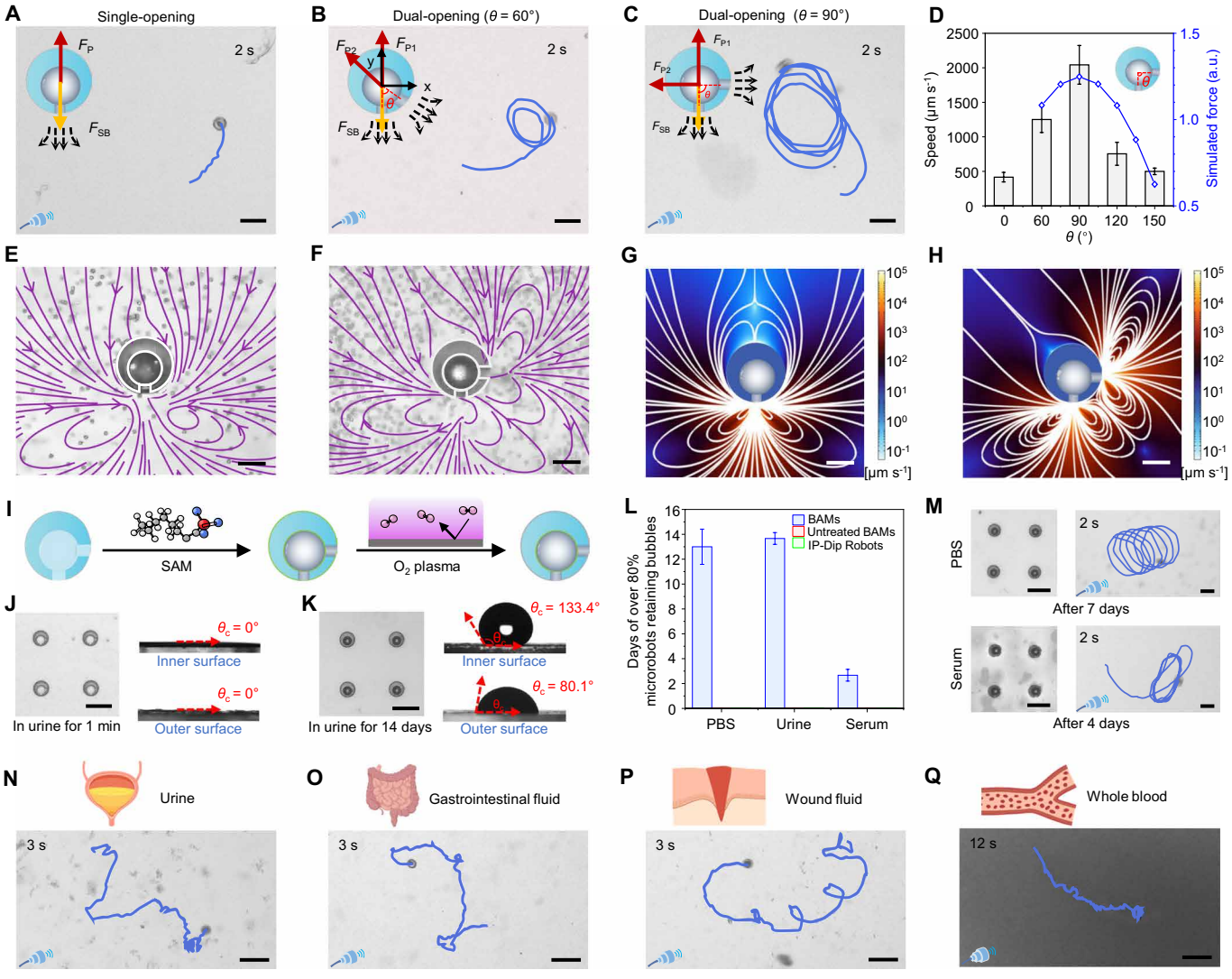

Fig. 2. Characterization of the propulsion of BAMs. (**A** to **C**) The propulsion trajectories of a single-opening BAM (A), a dual-opening (θ = 60°) BAM (B), and a dual-opening (θ = 90°) BAM (C). Scale bars, 50 μm. (**D**) The dependence of the experimentally measured velocity of BAMs and the simulated combined force on θ. Error bars represent the SD from 10 BAMs. a.u., arbitrary units. (**E** to **H**) The time-averaged streamline patterns of the vortex profiles of a single-opening BAM [(E) and (G)] and a dual-opening BAM [(F) and (H)] at the resonant frequency, obtained via PIV analysis of the passive particle tracers [(E) and (F)] and numerical simulation [(G) and (H)]. The BAM's body is fixed on the substrate with the opening parallel to the substrate. Scale bars, 15 μm. (**I**) Schematic illustration of the two-step surface treatment strategy to preserve microbubbles for extended periods in biofluids and maintain easy transferability. (**J** and **K**) Optical images of BAMs without (J) and with (K) the surface treatment after incubation in urine, and the corresponding θ_c values of the internal and external surfaces of BAMs. Scale bars, 50 μm. (**L**) Bubble-retaining capabilities in the biologically relevant fluids (i.e., PBS, urine, and serum) of 3D-printed microrobots based on IP-Dip, untreated BAMs, and surface-treated BAMs. Error bars represent the SD from three batches. (**M**) Optical images of the bubble-retaining BAMs and the motion trajectories of BAMs after being immersed in PBS for 7 days and in serum for 4 days. Scale bars, 50 μm. (**N** to **Q**) Schematics and motion trajectories of the microrobots in human urine (N), porcine gastrointestinal fluid (O), murine wound fluid (P), and whole blood (Q). Scale bars, 100 μm.

To overcome these obstacles and ensure stable in vivo operation, we adopted a unique surface chemistry approach aimed at preserving microbubbles for extended durations while facilitating the easy transfer and immersion of microrobots (Fig. 2I). Our strategy involved a two-step surface modification process. Initially, we treated BAMs with fluorosilane to create a highly hydrophobic self-assembled monolayer (SAM) on both the inner and outer surfaces. This hydrophobicity is essential for trapping bubbles; however, it also predisposes BAMs to self-aggregation and adherence to surfaces, complicating their deployment in fluids. To mitigate this, we subsequently applied a hydrophilic treatment via O_2 plasma etching to the SAM-coated BAMs, achieving a hydrophilic exterior while preserving the hydrophobic interior.

The experimental results indicate that this dual-step surface modification substantially enhanced microbubble stability. For example, unmodified hydrogel microrobots lost their bubbles within 1 min of immersion in biofluids such as urine, attributed to the hydrophilic PEGDA film's 0° contact angle (Fig. 2J). In contrast, the

modified BAMs, featuring a hydrophobic interior (with a contact angle of 133.4°) and a hydrophilic exterior (with a contact angle of 80.1°), successfully maintained microbubbles in human urine for 14 days (Fig. 2K).

Our comprehensive study on the durability of bubble retention in various microrobots fabricated through TPP further revealed BAMs' substantial improvements in bubble longevity. The microrobots based on traditional TPP resin IP-Dip lost their bubbles within 1 hour, and untreated hydrogel-based BAMs lost bubbles in 1 min in all tested biologically relevant fluids. In contrast, surface-treated BAMs demonstrated robust bubble retention, with over 80% of the BAMs sustaining bubbles for 3 days in serum, 12 days in PBS, and 13 days in urine (Fig. 2L and fig. S8). This extended bubble retention did not compromise BAMs' mobility, which remained efficient even after several days of immersion in various biofluids (Fig. 2M and fig. S9).

The unique asymmetric dual-opening design, combined with asymmetric surface hydrophobicity, was crucial for stabilizing microbubbles and ensuring robust operation within complex biological media. The BAMs exhibited the ability to navigate through untreated body fluids with varying viscosities—such as urine, gastrointestinal fluid, wound fluid, and whole blood—with high efficiency, achieving speeds of 896 ± 262, 812 ± 195, 621 ± 228, and 121 ± 19 μm s^{-1}, respectively (Fig. 2, N to Q; figs. S10 and S11; and movie S5). The trajectory of BAMs could be substantially influenced by the heterogeneity of biofluids. Moreover, the incorporation of the Fe_3O_4 NPs granted BAMs a superparamagnetic property (fig. S12), enabling precise control over the acoustic propulsion of a single BAM or a swarm of BAMs through an external magnetic field (fig. S13 and movie S6). These capabilities underscore BAMs' promising potential for real-world biomedical applications, demonstrating their effectiveness and adaptability in navigating the challenging environments of the human body.

Characterization of the material properties of BAMs

The main composition of BAMs is PEGDA, a US Food and Drug Administration–approved hydrogel material known for its nontoxicity and biodegradability. In aqueous environments, the hydrolysis of ester bonds within the cross-linked PEGDA framework triggers the breakdown of polymer chains, leading to the gradual degradation of BAMs (Fig. 3A) (*50*). This degradation process is notably faster under alkaline conditions because of enhanced hydrolysis via saponification. The hydrolytic degradation of BAMs was assessed in 50 mM NaOH, chosen for its minimal influence on human health (*51*). Routine optical inspections charted the degradation kinetics of BAMs, initially observing an expansion because of swelling followed by collapse within a 3-day period (Fig. 3B). The biocompatibility of Fe_3O_4 NPs and Fe_3O_4 NP–loaded BAMs was evaluated through incubating murine macrophage cells (RAW 264.7) and human bladder cancer (T24) cells with Fe_3O_4 NPs and passive BAMs, respectively. After a 72-hour incubation, both Fe_3O_4 NPs and BAMs exhibited negligible effects on the metabolic activity of the cells (Fig. 3, C and D, and fig. S14, A and B). The scant presence of red-stained dead cells further indicated BAMs' high compatibility with cellular environments (Fig. 3E and fig. S14C).

For therapeutic applications, the anticancer drug 5-FU was efficiently loaded into BAMs during the TPP fabrication process, facilitated by its minimal absorption at the TPP laser wavelength of 780 nm (*52*) and its low reactivity with photoinitiators (*53*). Given that the terminal half-life of 5-FU, when administered parenterally, is under 20 min because of rapid hepatic breakdown (*54*), encapsulation within BAMs substantially extends its half-life, thereby increasing its therapeutic efficacy. The drug-loading efficiency of BAMs was determined through ultraviolet-visible (UV-vis) spectroscopy, revealing that 1000 BAMs contained a total 5-FU dose of 183.1 ng. This amount represents 62.0% of the theoretical drug-loading capacity, on the basis of the maximum solubility of 5-FU in PEGDA resin (24 mg ml^{-1}), indicating effective drug incorporation within BAMs (fig. S15). The release profile of 5-FU from BAMs was monitored by observing the decrease in fluorescence intensity, with ~60% of the drug being released into urine within the initial 12 hours because of diffusion and polymer degradation (Fig. 3, F and G). Comparative analysis revealed that larger model drug molecules, such as rhodamine B, displayed a slower release rate, taking approximately 19 hours to achieve 60% release in human urine (fig. S16).

The in vitro therapeutic efficacy of 5-FU–loaded BAMs was assessed using a three-dimensional (3D) tumor spheroid model composed of T24 cells. This model closely simulates the mass transport dynamics and structural complexity of avascular tumor tissues (*55*–*57*). In the experiment, T24 spheroids, ~300 μm in diameter, were treated with PBS, 5 μM free drug, passive BAMs, or acoustically propelled BAMs carrying an equivalent amount of drug. After treatment, propidium iodide (PI) staining was applied to identify dead cells within the spheroids (Fig. 3H). The results revealed that acoustically propelled BAMs exhibited the strongest PI fluorescence intensities compared with the spheroids treated with PBS, free 5-FU, and passive BAMs (Fig. 3I). This can be attributed to the enhanced interaction between BAMs and tumor spheroids, a direct result of efficient propulsion of BAMs (fig. S17). This confirms the effectiveness of BAMs' propulsion and their polymer matrix in controlling drug release, substantially enhancing drug delivery efficiency and anticancer activity.

Ultrasound imaging of acoustically propelled BAMs in vitro and in vivo

The microbubbles trapped inside BAMs can increase the ultrasound imaging contrast, especially in deep tissue visualization. This is attributed to the acoustic impedance mismatch between air and water and the volumetric oscillations induced by microbubbles when exposed to ultrasound waves (Fig. 4A) (*45*, *46*). BAMs, whether individually or in arrays and across varying densities, can be efficiently detected and located within biological tissues or tissue-simulating phantoms using ultrasound imaging techniques (Fig. 4, B and C; fig. S18; and movie S7).

To achieve concurrent ultrasound imaging and acoustic propulsion of BAMs within soft tissue environments, a dual-probe approach was used. This approach comprises an ultrasound imaging probe for real-time imaging of the bubbles and a focused ultrasound (FUS) probe designed for effective propulsion. The choice of FUS over piezoelectric disks here is informed by its strong field at a low input voltage (fig. S19), which enhances its effectiveness and durability for the acoustic pressure amplitude attenuation through soft tissues (*58*). Adjusting the inner diameter of BAMs allows for the tuning of the resonant frequency of the trapped microbubbles to align with the FUS's center frequency, thereby maximizing operational efficiency (table S1 and fig. S20).

In vitro real-time imaging of the propulsion of BAMs was conducted within an agarose chamber, simulating a bladder environment

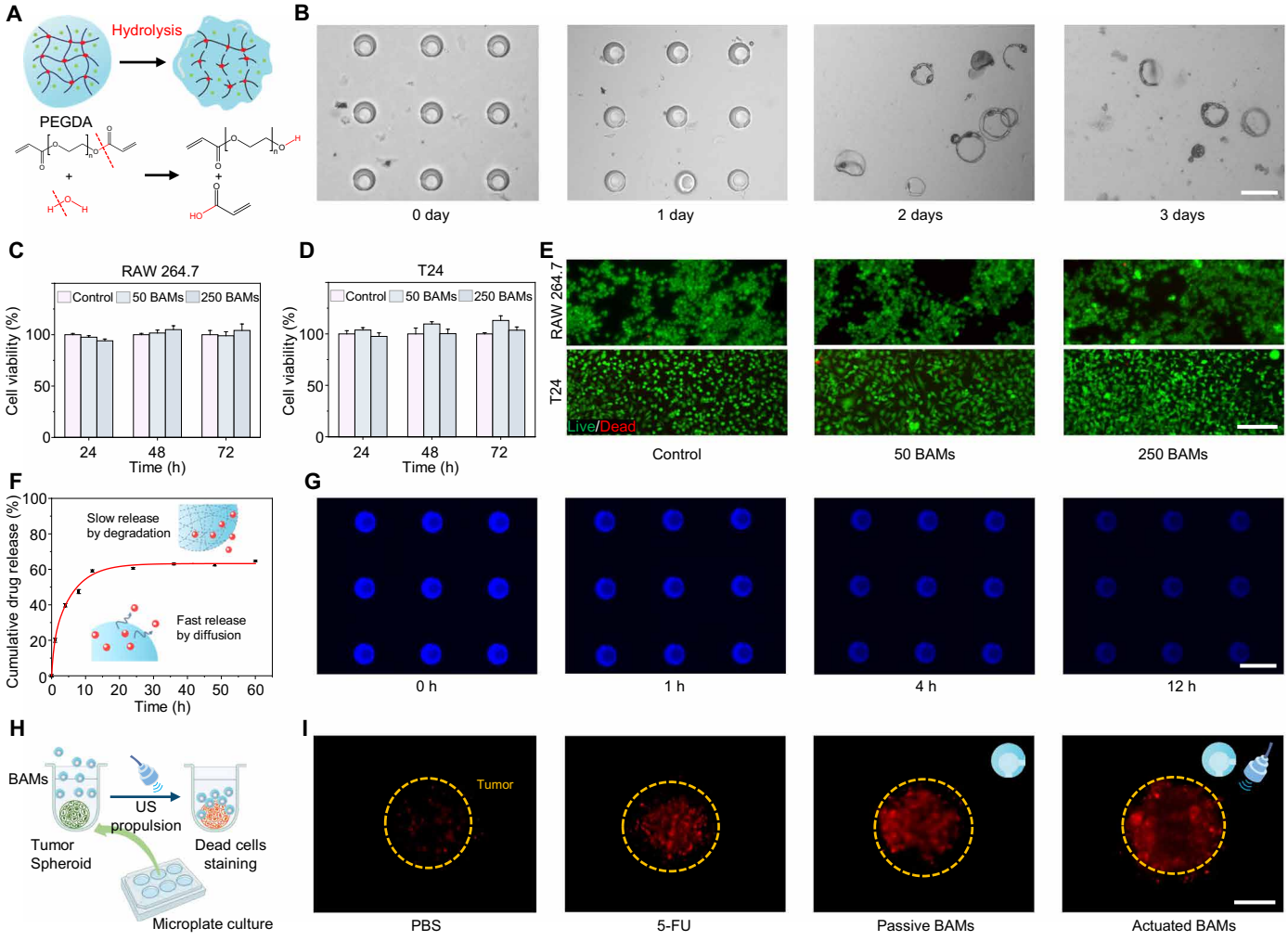

Fig. 3. In vitro evaluation of biodegradability, drug release, and biocompatibility of BAMs. (**A**) Schematic of the degradation mechanism of PEGDA, the backbone material of BAMs. (**B**) Bright-field microscopic images demonstrating the degradation of BAMs to debris within 3 days in 50 mM NaOH. Scale bar, 50 μm. (**C** and **D**) Cell viability of RAW 264.7 (C) and T24 (D) cells cocultured with BAMs. Error bars represent the SD of four measurements. (**E**) Representative live (green)/dead (red) fluorescence images of RAW 264.7 (top) and T24 cells (bottom) seeded with PBS (control) and BAMs after 3 days of culture. Scale bar, 100 μm. (**F**) The time-dependent cumulative drug release of 5-FU from BAMs in urine. (**G**) Fluorescence images of the time-dependent release of 5-FU from BAMs in urine. Scale bar, 50 μm. (**H**) Schematic of the in vitro tumor spheroid treatment process using BAMs. (**I**) Representative fluorescence images of dead cells (red color) stained with PI dye in T24 spheroids after a 15-min exposure to PBS, 5 μM 5-FU, nonactuated BAMs, and acoustically actuated BAMs, respectively, followed by washing and a 48-hour incubation. The outline depicts the shape of the spheroid at its largest cross section. Scale bar, 100 μm.

and using a 50-MHz linear array ultrasound probe in the B-mode imaging configuration (Fig. 4, D to G). The propulsion of BAMs, facilitated by the ultrasound field generated by the FUS probe at an excitation frequency of 480 kHz and an applied acoustic pressure of 626 kPa (peak-to-peak pressure), was observed. BAMs with an inner diameter of 14 μm, which have a resonant frequency close to the excitation frequency (table S1), demonstrated highly efficient motion, as captured in ultrasound imaging scans (Fig. 4E and movie S8). Guided by the ultrasound imaging, the propulsion direction of BAMs can be precisely and wirelessly controlled by an external magnetic field, leveraging their superparamagnetic properties (Fig. 4, F and G, and movie S8).

The evaluation of in vivo propulsion and imaging of BAMs was conducted within the mouse bladder using the capabilities of a setup that aligns ultrasound propulsion and imaging (fig. S21). This setup ensured that the imaging probe's central axis intersected the focal point of the propulsion transducer, hence aligning the ultrasound imaging zone with the propulsion field. BAMs were administered into the mouse bladder through intravesical instillation, demonstrating vortex-like motion upon activation by ultrasound (movie S9). Ultrasound imaging revealed that, under magnetic control, BAMs moved toward a specific bladder region (Fig. 4, H to K, and movie S9). The potential of BAMs for in vivo tumor targeting was assessed in a mouse with orthotopic bladder cancer. Ultrasound imaging enabled the visualization of the bladder tumor, aiding in the precise delivery of BAMs to the tumor site via acoustic propulsion coupled with magnetic steering (Fig. 4, L and M, and movie S10). Once attached to the tumor tissue or

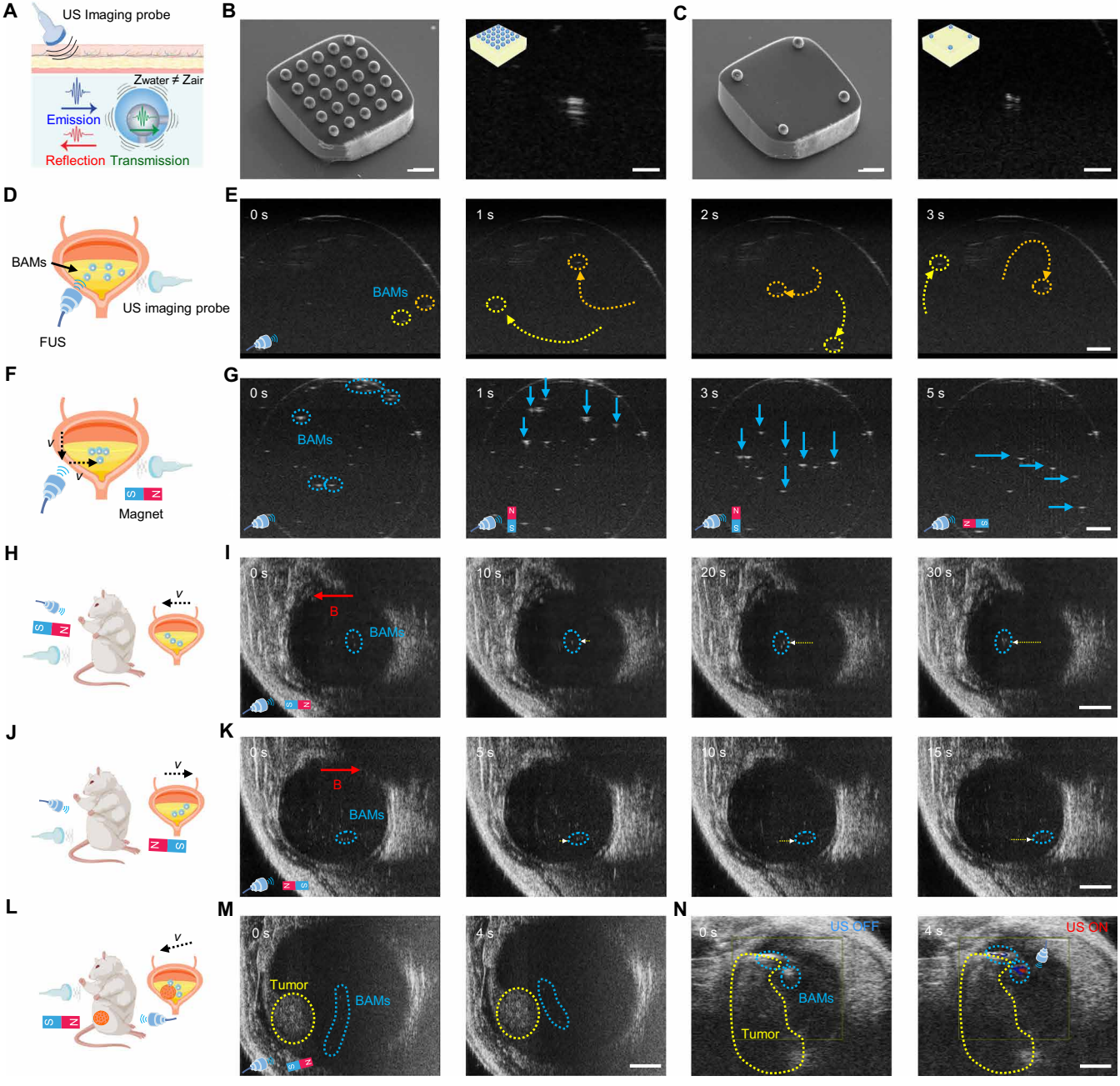

Fig. 4. Characterization of the propulsion, control, and imaging of BAMs in vitro and in vivo. (**A**) Schematic of deep-tissue ultrasound imaging of a BAM with the trapped microbubble serving as the contrast agent. (**B** and **C**) SEM and ultrasound images of BAM arrays with varied densities: one BAM per 50 μm^2 by 50 μm^2 (B) and 200 μm^2 by 200 μm^2 (C). Scale bars, 50 and 500 μm for SEM and ultrasound images, respectively. (**D** to **G**) Schematics and the corresponding ultrasound images of in vitro acoustic propulsion of BAMs without [(D) and (E)] and with [(F) and (G)] magnetic guidance in an agarose chamber–based artificial bladder. Scale bars, 1 mm. (**H** to **K**) Schematics and the corresponding ultrasound images of propulsion of BAMs with magnetic guidance to the left side [(H) and (I)] and right side [(J) and (K)] in vivo in the bladder of a mouse. Scale bars, 2 mm. (**L** and **M**) Schematic and the corresponding ultrasound images of acoustic propulsion-based, magnetically navigated tumor targeting of BAMs in vivo in a mouse bladder with orthotopic bladder tumor. Scale bar, 2 mm. (**N**) Doppler mode ultrasound images of BAMs remaining attached to the tumor despite alterations in magnetic orientation while retaining responsiveness to ultrasound stimuli. Scale bar, 2 mm.

embedded within the bladder wall, BAMs remained firmly in place and ultrasound responsive despite changes in magnetic direction. The enduring attachment and responsiveness were verified through Doppler mode ultrasound imaging (Fig. 4N).

Evaluation of the anticancer therapeutic efficacy of BAMs in vivo

The therapeutic efficacy of BAMs was assessed in vivo through a murine orthotopic bladder tumor model established by the inoculation

of luciferase-expressing murine bladder carcinoma cells (MB49) into mice over a 7-day period (Fig. 5A). Tumor-bearing mice received intravesical instillation of either PBS, free drug, passive BAMs, or acoustically actuated and magnetically guided BAMs at 3-day intervals over four sessions. Tumor progression was monitored via the bioluminescence signal emitted by MB49 cells throughout the treatment period of 21 days (Fig. 5, B and C). By the 14th day after beginning BAM treatment, an ~93% decrease in bioluminescence was observed in the FUS-actuated BAM group, indicating a large reduction in tumor sizes. In contrast, groups treated with free 5-FU or passive BAM showed a less complete reduction in bioluminescence relative to PBS-treated controls. Analysis of the bladders resected at the study end point revealed that mice treated with BAMs had the smallest bladder sizes, indicating the smallest tumor volumes (Fig. 5D). Further histological examination of the excised whole bladders using hematoxylin and eosin (H&E) staining demonstrated considerably reduced tumor sizes in the BAM-treated mice (Fig. 5E), underscoring the efficacy of BAMs for effective tumor suppression.

In addition to the therapeutic efficacy, the biocompatibility of BAMs during the in vivo treatment was evaluated. No substantial changes in body weights were observed among all of the mice (Fig. 5F), and histological examination of major organs (i.e., heart, liver, spleen, lung, and kidney) indicated no adverse influence when compared to the control group treated with PBS (Fig. 5G). Furthermore, the in vivo degradability of BAMs was evaluated by subcutaneous implantation of BAMs into both flanks of a mouse, which offered a realistic environment for evaluating microrobot bioresorption. Histological analysis at 4 weeks after implantation showed a gradual decrease in microrobot size, with

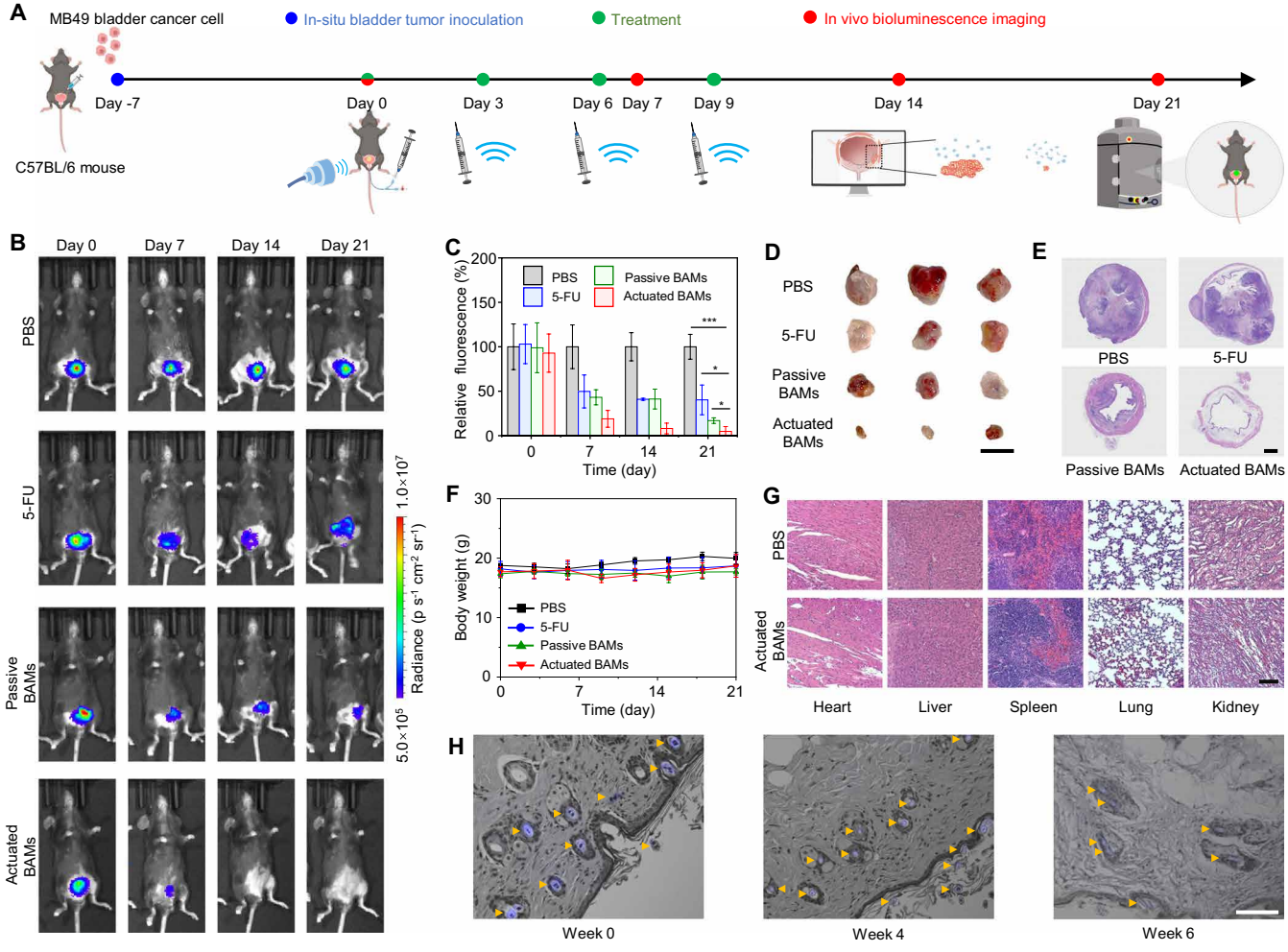

Fig. 5. In vivo evaluation of the therapeutic efficacy, biosafety, and biodegradation of BAMs using an orthotopic bladder tumor model. (**A**) Schematic of the study protocol in establishing orthotopic MB49 bladder tumors in C57BL/6 J mice, followed by treatment (green dots) and imaging (red dots) procedures. (**B** and **C**) Representative in vivo imaging system (IVIS) images of the luciferase-expressing MB49 bladder tumor-bearing mice (B) and quantified relative bioluminescence intensity (C) upon various intravesical administrations over the treatment course, including PBS, 5-FU, passive BAMs, and acoustically actuated BAMs on days 0, 7, 14, and 21. Error bars in (C) represent the SD from three mice (*$P < 0.05$; ***$P < 0.001$). (**D**) Images of bladder size at the end of the study for each group. Scale bar, 1 cm. (**E**) H&E staining of bladder cross sections from MB49 tumor–bearing mice of different groups at the end of the study. Scale bar, 1 mm. (**F**) Body weights of mice in different groups during the whole treatment process (21 days). (**G**) H&E staining of histological sections of the mice in the control group and the acoustically actuated BAM group. Heart, liver, spleen, lung, and kidney tissues were collected at the end of the study. Scale bar, 100 μm. (**H**) Fluorescence images of BAMs after 0, 4, and 6 weeks of subcutaneous implantation. Blue color indicates BAMs. Scale bar, 50 μm.

complete breakdown observed by the sixth week (Fig. 5H). Collectively, these results support the safe use of BAMs for in vivo applications, highlighting their efficacy in tumor reduction and their biocompatible and bioresorbable nature.

DISCUSSION

BAMs represent a powerful tool in precision medicine, addressing challenges that have historically hindered the practical application of synthetic micro- and nanorobots. BAMs also demonstrate substantial advances compared with previously developed magnetically steered, ultrasound driven microrobots (table S2). With the ability to maintain propulsion in various biological fluids for several days and exhibit strong real-time imaging contrast, these devices demonstrate the potential to shift paradigms in disease diagnosis, targeted drug delivery, and minimally invasive surgery. Specifically, the use of high-resolution TPP in their fabrication, alongside the integration of Fe_3O_4 NPs for magnetic navigation, enables a level of maneuverability and functional sophistication that is unparalleled in contemporary therapeutic interventions. In addition, the design featuring a cavity with two openings notably boosts the propulsion efficiency of BAMs in complex biofluids. Moreover, a two-step surface treatment method tackles the problems of transient stability and short life span of bubbles within these fluids.

Modifications to the surface chemistry, conferring BAMs with both hydrophobic and hydrophilic characteristics, markedly improved their durability and compatibility with biofluids. This innovation greatly extended the microbubbles' life span within the BAMs, which is essential for their propulsion and imaging capabilities. Such advancements enable BAMs to navigate and function within the human body more efficiently and for longer durations, marking a substantial leap from previous models by facilitating sustained operation in biological environments without frequent reintervention.

The integration of hydrogel as the core material of BAMs presents substantial benefits for biomedical applications in vivo. In a bladder cancer model, embedding the anticancer drug 5-FU into the hydrogel matrix of BAMs substantially improved the therapeutic efficiency compared with 5-FU alone. These BAMs used a controlled-release mechanism that prolonged the bioavailability of the loaded drug, leading to sustained therapeutic activity and better outcomes. In addition, the hydrogel's biodegradability through hydrolysis presents another critical advantage for in vivo applications. This property ensures the safety and biocompatibility of these microrobots, obviating the need for their surgical extraction after treatment. Consequently, this could reduce patient risk and simplify the posttreatment protocol, further highlighting the utility and potential of BAMs in modern medicine.

Looking forward, the successful application of BAMs in clinical settings will crucially depend on the ability to produce these materials at scale and the flexibility of their design to meet the diverse therapeutic requirements across different parts of the body. As BAM technology progresses, we anticipate that it will have the potential to make a substantial impact on the health care sector and patient care.

MATERIALS AND METHODS

Materials

PEGDA (number-average molecular weight, 575; 437441), PETA, 5-FU (343922), dichloromethane (DCM), dimethyl sulfoxide, 3-(trimethoxysilyl) propyl methacrylate (M6514), trichloro(1*H*,1*H*,2*H*,2*H*-perfluorooctyl) silane, rhodamine B, and calcein AM/ethidium were obtained from Sigma-Aldrich. Ethanol, toluene, 10× PBS, sodium hydroxide, and glass coverslips were purchased from Thermo Fisher Scientific. Iron(II,III) oxide magnetic NP solution (Fe_3O_4 NPs, 50-nm average size, PEG-amine functionalized, Chemicell GmbH), and 7-diethylamino-3-thenoylcoumarin (DETC) were acquired from Combi-Blocks. In addition, 2-μm polystyrene microparticle solution was ordered from microParticles GmbH. Paraformaldehyde solution was purchased from Electron Microscopy Sciences. Dulbecco's modified Eagle's medium (DMEM) was obtained from American Type Culture Collection (ATCC). Penicillin and streptomycin were obtained from Lonza.

Fabrication of BAMs

Preparation of printing resin

PEG-functionalized Fe_3O_4 NPs were added to a PEGDA-PETA mixture (90%:10%, v/v) to reach a final concentration of 3 mg ml^{-1}, and the resultant resin was sonicated for 20 min. DETC (3 mg in 20 μl DCM), a photoinitiator, was added to 300 μl of resin and vortex-mixed for 2 min. 5-FU was dissolved in dimethyl sulfoxide at a concentration of 100 mg ml^{-1}, which was added to the resin to achieve a final concentration of 24 mg ml^{-1}. For BAMs containing the model drug, rhodamine B was dissolved in DCM at a level of 10 mg ml^{-1} and was added to the resin to achieve a final concentration of 1 mg ml^{-1}.

3D printing of BAMs

A glass substrate, 30 mm in diameter (NanoScribe GmbH), was immersed in 3-(trimethoxysilyl)propyl methacrylate solution [1% (v/v) in ethanol] for 45 min, rinsed in water, and dried with nitrogen to enhance the surface adhesion of the prepared photoresist. Next, 50 μl of the prepared resin (PEGDA-PETA/DETC/5-FU/Fe_3O_4) was dropped onto the treated glass substrate and was loaded into a 3D laser lithography tool (NanoScribe GmbH, Germany). BAMs were lastly fabricated using a 63× oil immersion objective (numerical aperture of 1.4 from Zeiss). After the photopolymerization, uncured photoresist was removed using isopropyl alcohol for 15 min and was dried with nitrogen.

Surface modification

BAMs were first activated in an oxygen plasma chamber at 100 W for 1 min (Plasma Etch Inc.) and then fluorosilanized with 20 μl of trichloro(1*H*,1*H*,2*H*,2*H*-perfluorooctyl)silane for 20 min under 80°C in a vacuum oven (Model 281A, Fisherbrand), followed by a 15-s oxygen plasma process.

Material characterization of BAMs

The morphologies of the microrobots were obtained using scanning electron microscopy (SEM; ZEISS 1550VP FESEM). The device was equipped with an energy-dispersive x-ray spectroscopy analyzer (Oxford X-Max SDD) to determine the element composition of BAMs. The bright-field and fluorescence images were captured with an inverted Zeiss AXIO optical microscope.

The paramagnetic properties of BAMs were characterized using a vibrating sample magnetometer (Microsense EZ7). The hysteresis loop plot obtained on 1000 fabricated BAMs indicated a maximum magnetization value of 2.6×10^{-4} emu in the range of −0.5 to 0.5 T and a coercive field of 0.064 mT.

To characterize the hydrophobicity of BAMs, PEGDA thin film was printed on glass slides, followed by different surface treatments

for the contact angle measurement. The surface contact angles were acquired using a goniometer (ramé-hart).

Microstreaming simulation and visualization

The numerical simulations reported in this work were conducted using the commercial COMSOL Multiphysics finite element software. A detailed description can be found in Supplementary Methods. To validate the simulation of microstreaming trajectories, 2-μm polystyrene tracer particles were mixed in the medium to generate the distribution of the streaming patterns. The videos were recorded using a high-speed camera (Axiocam 702 mono, Zeiss) at 150 frames s^{-1} (fps). Subsequently, the videos were analyzed with MATLAB (PIVlab) software.

Bubble life span of BAMs

To evaluate the bubble-retaining capability of BAMs in biofluids, serum was obtained from ATCC, and porcine gastrointestinal fluid was obtained from Sierra Medical Company. Wound fluid was obtained from Zucker diabetic fatty obese fa/fa diabetic rats (the Jackson Laboratory, Bar Harbor, ME, USA). Whole blood and urine were collected from a healthy human participant after securing written informed consent, in accordance with the approved protocol IR24-0892. BAM arrays were submerged in biofluids. Arrays were imaged using the optical microscope to check the bubble status. The long-term propulsion stability test of BAMs was performed after being immersed in PBS for 0, 2, 4, and 7 days. To evaluate the biodegradability of BAMs in vitro, arrays of BAMs were immersed in 50 mM NaOH solution within petri dishes and stored in a 37°C incubator.

Characterization of the propulsion of BAMs in vitro

To test the propulsion of BAMs under the microscope, a piezoelectric disk transducer was mounted onto a transparent glass slide through which ultrasound waves were transmitted and then radiated into the solution on the cover slide. A sinusoidal driving signal was generated using an arbitrary function generator in burst mode with the central frequencies of the transducers. The electrical signals (100 to 300 mV) from the function generator were amplified with a high-voltage amplifier (HA-820A, Pintech) with a gain of 40 dB and zero offset to power the disk transducer.

The propulsion of microrobots in vitro was recorded by a high-speed camera (Axiocam 702 mono, Zeiss) at 50 fps, and the trajectories were visualized via the Manual Tracking and MTrack2 plugins of ImageJ (version 1.54f). The velocity calculation for microrobots was performed using Video Spot Tracker (version 08.01). The velocity of the entire trajectory was averaged among all of the time steps. The rheological properties of the different biofluids were analyzed using a rheometer (MCR 302, Anton Paar).

To investigate the locomotion of BAMs near the wall, the wall was made of polypropylene box with grooves. A gene frame was attached to the bottom of the box and covered with a plastic film. The probe transducer was used to propel the BAMs.

For applications involving soft tissues, an FUS probe transducer (TQ60-0560, Siansonic Technology Ltd., Beijing, China) with a center frequency of 480 kHz through hydrophone characterization was used. The transducer exhibited a focal region precisely centered at 52.68 mm, with a focal length of ~15 mm and a focal width of about 4.5 mm. The electrical signal from the function generator was amplified by a power amplifier (Model 75A250, Amplified Research, Souderton, PA) with a gain of 50 dB to power the FUS.

Experimental calibration of the FUS transducer was performed in degassed water (Aquas-10 water conditioner, Onda Corporation, Sunnyvale, CA). The transducer was connected to a BiSlide computer-controlled 3D translatable stage (Velmex, Bloomfield, NY), and acoustic pressure fields were measured using a needle hydrophone (HNR-0500, Onda Corporation, Sunnyvale, CA) with traceable calibration between 0.3 and 20 MHz at 50-kHz intervals. Sinusoidal input signals were generated with a 5-MHz waveform generator (4052 model, BK Precision Corp., Yorba Linda, CA) and amplified with a high-frequency amplifier (Model 75A250, Amplified Research, Souderton, PA). Voltage across the transducer was monitored using a high-voltage oscilloscope probe (P4250 100:1 2KV 250 MHz, Goupchn) connected between the high-frequency amplifier and the transducer. All signals were recorded using a digital oscilloscope (InfiniiVision DSOX2004A, Keysight Technologies, Santa Rosa, CA).

Evaluation of the drug loading and release capabilities of BAMs

The loaded 5-FU amount in BAMs was quantified by measuring the absorption at 293 nm by UV-vis spectrometry with NanoDrop after fully dissolving BAMs in 0.5 M NaOH. The drug-loading efficiency was determined as the ratio of the loaded 5-FU in BAMs and the dissolved 5-FU in the resin (24 mg ml^{-1}) with the same volume as the final BAMs. The drug release was measured with a fluorescence microscope and analyzed by ImageJ.

In vitro cellular and tissue studies

Cell lines

T24 cancer cells (ATCC) and RAW 264.7 macrophage cells (ATCC) were cultured in DMEM under 37°C and 5% CO_2. Cells were passaged at 75% confluency and three to five times for all studies.

In vitro tumor spheroid treatment

In total, 5×10^3 T24 cancer cells were seeded into each well of a 96-well microplate with a cell-repellent surface (Greiner Bio-One GmbH) in 100 μl of DMEM containing 10% fetal bovine serum and 1% penicillin/streptomycin (Lonza). T24 cells transitioned from loose aggregates to highly compact 3D spheroids after 3 days of culture. BAMs were sterilized in ethanol for 2 min and dried under a N_2 flow. The spheroids were then exposed to PBS, 5-FU in PBS, passive BAMs, and actuated BAMs for 15 min. For the actuated BAM group, a piezoelectric transducer was attached to the bottom of the well plate to propel BAMs for 5 min at the beginning of incubation. The spheroids were washed with Dulbecco's PBS (DPBS) after incubation to minimize the potential residues of the free drug. The optical and fluorescence images were taken to compare the interaction of passive and actuated BAMs with tumor spheroids. After 48 hours of incubation, the spheroids were stained with calcein AM/ethidium homodimer-1 live/dead (Invitrogen) and then were washed with DPBS twice. A fluorescein isothiocyanate channel was used to observe the live cells (green), and a cyanine 3 channel was used to observe the dead cells (red) under fluorescence light-emitting diode illumination (X-Cite 120LEDmini, Excelitas Technologies).

Cytotoxicity

A total of 5×10^3 RAW 264.7 cells were seeded into a 96-well microplate in DMEM containing 10% fetal bovine serum and 1% penicillin/streptomycin. After 24 hours, BAMs and Fe_3O_4 NPs (0, 2, or 4 μg ml^{-1}) were added to the corresponding groups, respectively. Before addition, BAMs and Fe_3O_4 NPs were exposed to UV light for 30 min

for disinfection. The cells were incubated with BAMs and Fe_3O_4 NPs for 3 days, and the cell viability was measured each day with PrestoBlue (Invitrogen) reagent. The fluorescence intensity of each group was obtained using a microplate reader (Synergy HTX, BioTek). Cell viability (%) was calculated as (mean intensity of the experimental group − mean intensity of the blank group) / (mean intensity of the control group − mean intensity of the blank group) × 100%. After 3 days, the cells were washed with DPBS and then stained with the live/dead dye, and the fluorescence images were captured using the fluorescein isothiocyanate and cyanine 3 channels for live and dead cells, respectively. The acquired images were further analyzed using ImageJ.

Real-time ultrasound imaging of BAMs in vitro and in vivo

In vitro propulsion and ultrasound imaging

An agarose chamber was used as the artificial bladder for in vitro evaluation. A 3D-printed coupling cone was specifically designed to ensure proper alignment between the artificial bladder and the transducer. Real-time videos of BAMs were recorded using a high-frequency ultrasound imaging system (Vevo 2100 imaging system, FUJIFILM VisualSonics Inc.) with a 50-MHz linear array ultrasound probe (MS700) and operating in the B-mode imaging configuration. The acoustic waves for propulsion were set at an excitation frequency of 480 kHz, applying acoustic pressure at approximately 626 kPa (peak-to-peak value). To demonstrate that BAMs can be observed with lower-frequency imaging probes, a Vantage 256 ultrasound system (Verasonics Inc., Seattle, USA) with an L22-14v imaging probe running at a frequency of 15.625 MHz was used for in vitro imaging in a capillary tube filled with flowing PBS under a 1-cm-thick chicken breast (fig. S18).

In vivo propulsion and ultrasound imaging

In this case, it is imperative to ensure that the ultrasound propulsion field is properly applied to the targeted region. A coaligned propulsion and imaging setup is essential to guarantee the congruence of the ultrasound imaging area with the application zone of the ultrasound propulsion field. The design principle of this coaligned setup is to maintain the imaging probe's median line passing through the focal center of the propulsion transducer (fig. S21). The imaging probe and FUS were mounted perpendicularly on a customized 3D-printed holder. The focal point of the FUS was precisely aligned at the center of the imaging probe, with a depth setting of 5 mm. This alignment ensures that when the bladder is visualized on the display at a distance of 5 mm from the imaging probe, the propulsion field is concurrently applied to the identical location. Mice were anesthetized with 5% isoflurane in pure O_2 and maintained under anesthesia in the mouse holder for the entire imaging procedure. The hair over the abdomens of the tumor-bearing mice was removed. The tumor-bearing mice were intravesically instilled with BAMs. The integrated system and the abdomens of the mice were submerged in a 37°C water tank. To increase the magnetic response, BAMs were immersed in a water suspension of PEG-functionalized Fe_3O_4 NPs (4 mg ml^{-1}; 30-nm mean size; Sigma-Aldrich) for 1 hour. Magnets were used for real-time navigation, whereas the imaging and propulsion were activated.

Animal studies

Animal type and cell line

To evaluate the in vivo therapeutic efficacy of BAMs, a murine bladder mouse model was used. C57BL/6J (the Jackson Laboratory), 8-week-old female mice were used for the animal studies. For the tumor model, murine bladder carcinoma cells transfected with luciferase (MB49-Luc, Applied Biological Materials Inc.) were cultured under 37°C and 5% CO_2. Cells were passaged at 75% confluency and three to five times for all studies. All animal studies were approved by the Institutional Animal Care and Use Committee (protocol Nos. IA23-1800 and IA23-1859) at California Institute of Technology and were conducted strictly in compliance with guidelines and protocols for proper animal care.

In vivo bladder cancer treatment

The murine tumor model was established by orthotopically injecting MB49-Luc (5×10^4 cells in 20 μl of DPBS) into the bladder wall of each anesthetized mouse via a 31-gauge insulin syringe (BH Supplies). Seven days after the tumor inoculations (day 0), the mice were randomly divided into four treatment groups ($n = 3$), and the treatment was started. The mice were anesthetized, and body weights were recorded. On days 0, 3, 6, and 9, the mice were intravesically treated with 200 μl of PBS, 5 μM 5-FU, 700 passive BAMs, and 700 actuated BAMs through a closed IV catheter system (0.7 mm by 19 mm; BD Intima II). After incubation for 20 min, mice were recovered from anesthesia. On day 21, all of the mice were euthanized, and the organs were harvested and stored in 4% paraformaldehyde. An in vivo imaging system (IVIS, Lumina Series III, PerkinElmer) was used to monitor the bioluminescence of tumors.

Histological evaluations

The harvested tissues were rinsed with DPBS (5×) and then incubated in 30% sucrose overnight (4°C). Samples were mounted in optimal cutting temperature compound (Thermo Fisher Scientific), followed by flash-freezing and cryosectioning (50-μm sections). The sections were embedded in paraffin, fixed on microscope slides, and stained with H&E staining. To remove the paraffin, cryosections were immersed in xylene for two cycles with each cycle lasting 10 min, followed by two rounds of 5-min hydration using 100% ethanol. The sections were then briefly immersed in 95 and 70% ethanol for 1 min each, followed by rinsing in deionized water. Next, the sections were submerged in filtered Harris hematoxylin for 10 s. The rack containing the sections was transferred to a beaker of water to dilute the dye. The sections were submerged in eosin stain for ~30 s and then transferred to the beaker with fresh water for rinsing. Two cycles of 5-min 100% ethanol immersion were performed to dehydrate the sections. In addition, two cycles of 5-min xylene immersion were conducted to clear the sections. Last, the sections were fixed using resin-based mounting medium.

In vivo biodegradation and biocompatibility

A total of 100 BAMs were subcutaneously implanted into the left and right flanks of the mice through a 10-mm incision. At weeks 0, 4, and 6, the mice were euthanized, and the subcutaneous tissue with embedded BAMs was collected. The excised tissue was fixed in 4% paraformaldehyde for sectioning and H&E staining. BAM-embedded tissue was imaged using a fluorescence microscope.

Statistical analysis

Quantitative data were illustrated as means ± SD. Comparison between multiple groups was performed using one-way analysis of variance (ANOVA) with a Tukey post hoc test. Statistical significance of the IVIS results was represented as $*P < 0.05$, $**P < 0.01$, and $***P < 0.001$.

Supplementary Materials

The PDF file includes:
Methods
Figs. S1 to S21
Tables S1 and S2
Legends for movies S1 to S10
References (*59*–*65*)

Other Supplementary Material for this manuscript includes the following:
Movies S1 to S10
MDAR Reproducibility Checklist

REFERENCES AND NOTES

1. J. Li, B. E.-F. de Avila, W. Gao, L. Zhang, J. Wang, Micro/nanorobots for biomedicine: Delivery, surgery, sensing, and detoxification. *Sci. Robot.* **2**, eaam6431 (2017).
2. B. J. Nelson, S. Pané, Delivering drugs with microrobots. *Science* **382**, 1120–1122 (2023).
3. F. Zhang, J. Zhuang, Z. Li, H. Gong, B. E.-F. De Ávila, Y. Duan, Q. Zhang, J. Zhou, L. Yin, E. Karshalev, W. Gao, V. Nizet, R. H. Fang, L. Zhang, J. Wang, Nanoparticle-modified microrobots for in vivo antibiotic delivery to treat acute bacterial pneumonia. *Nat. Mater.* **21**, 1324–1332 (2022).
4. C. Simó, M. Serra-Casablancas, A. C. Hortelao, V. Di Carlo, S. Guallar-Garrido, S. Plaza-García, R. M. Rabanal, P. Ramos-Cabrer, B. Yagüe, L. Aguado, L. Bardia, S. Tosi, V. Gómez-Vallejo, A. Martín, T. Patiño, E. Julián, J. Colombelli, J. Llop, S. Sánchez, Urease-powered nanobots for radionuclide bladder cancer therapy. *Nat. Nanotechnol.* **19**, 554–564 (2024).
5. Z. Wu, L. Li, Y. Yang, P. Hu, Y. Li, S.-Y. Yang, L. V. Wang, W. Gao, A microrobotic system guided by photoacoustic computed tomography for targeted navigation in intestines in vivo. *Sci. Robot.* **4**, eaax0613 (2019).
6. B. E.-F. De Ávila, P. Angsantikul, J. Li, M. A. Lopez-Ramirez, D. E. Ramírez-Herrera, S. Thamphiwatana, C. Chen, J. Delezuk, R. Samakapiruk, V. Ramez, M. Obonyo, L. Zhang, J. Wang, Micromotor-enabled active drug delivery for in vivo treatment of stomach infection. *Nat. Commun.* **8**, 272 (2017).
7. F. Zhang, Z. Li, Y. Duan, A. Abbas, R. Mundaca-Uribe, L. Yin, H. Luan, W. Gao, R. H. Fang, L. Zhang, J. Wang, Gastrointestinal tract drug delivery using algae motors embedded in a degradable capsule. *Sci. Robot.* **7**, eabo4160 (2022).
8. J. Yoo, S. Tang, W. Gao, Micro- and nanorobots for biomedical applications in the brain. *Nat. Rev. Bioeng.* **1**, 308–310 (2023).
9. R. Nauber, S. R. Goudu, M. Goeckenjan, M. Bornhäuser, C. Ribeiro, M. Medina-Sánchez, Medical microrobots in reproductive medicine from the bench to the clinic. *Nat. Commun.* **14**, 728 (2023).
10. H. Zhang, Z. Li, C. Gao, X. Fan, Y. Pang, T. Li, Z. Wu, H. Xie, Q. He, Dual-responsive biohybrid neutrobots for active target delivery. *Sci. Robot.* **6**, eaaz9519 (2021).
11. S. Jeon, S. Kim, S. Ha, S. Lee, E. Kim, S. Y. Kim, S. H. Park, J. H. Jeon, S. W. Kim, C. Moon, B. J. Nelson, J. Kim, S.-W. Yu, H. Choi, Magnetically actuated microrobots as a platform for stem cell transplantation. *Sci. Robot.* **4**, eaav4317 (2019).
12. X. Wang, Z. Gong, T. Wang, J. Law, X. Chen, S. Wanggou, J. Wang, B. Ying, M. Francisco, W. Dong, Y. Xiong, J. J. Fan, G. MacLeod, S. Angers, X. Li, P. B. Dirks, X. Liu, X. Huang, Y. Sun, Mechanical nanosurgery of chemoresistant glioblastoma using magnetically controlled carbon nanotubes. *Sci. Adv.* **9**, eade5321 (2023).
13. C. Chen, S. Ding, J. Wang, Materials consideration for the design, fabrication and operation of microscale robots. *Nat. Rev. Mater.* **9**, 159–172 (2024).
14. H. Zhou, C. C. Mayorga-Martinez, S. Pané, L. Zhang, M. Pumera, Magnetically driven micro and nanorobots. *Chem. Rev.* **121**, 4999–5041 (2021).
15. R. Dong, Y. Cai, Y. Yang, W. Gao, B. Ren, Photocatalytic micro/nanomotors: From construction to applications. *Acc. Chem. Res.* **51**, 1940–1947 (2018).
16. Y. Alapan, O. Yasa, B. Yigit, I. C. Yasa, P. Erkoc, M. Sitti, Microrobotics and microorganisms: Biohybrid autonomous cellular robots. *Annu. Rev. Control Robot. Auton. Syst.* **2**, 205–230 (2019).
17. L. Xu, F. Mou, H. Gong, M. Luo, J. Guan, Light-driven micro/nanomotors: From fundamentals to applications. *Chem. Soc. Rev.* **46**, 6905–6926 (2017).
18. S. Tottori, L. Zhang, F. Qiu, K. K. Krawczyk, A. Franco-Obregón, B. J. Nelson, Magnetic helical micromachines: Fabrication, controlled swimming, and cargo transport. *Adv. Mater.* **24**, 811–816 (2012).
19. Z. Wu, Y. Chen, D. Mukasa, O. S. Pak, W. Gao, Medical micro/nanorobots in complex media. *Chem. Soc. Rev.* **49**, 8088–8112 (2020).
20. M. Medina-Sánchez, O. G. Schmidt, Medical microbots need better imaging and control. *Nature* **545**, 406–408 (2017).
21. C. K. Schmidt, M. Medina-Sánchez, R. J. Edmondson, O. G. Schmidt, Engineering microrobots for targeted cancer therapies from a medical perspective. *Nat. Commun.* **11**, 5618 (2020).
22. X. Yan, Q. Zhou, M. Vincent, Y. Deng, J. Yu, J. Xu, T. Xu, T. Tang, L. Bian, Y.-X. J. Wang, K. Kostarelos, L. Zhang, Multifunctional biohybrid magnetite microrobots for imaging-guided therapy. *Sci. Robot.* **2**, eaaq1155 (2017).
23. Q. Wang, Q. Wang, Z. Ning, K. F. Chan, J. Jiang, Y. Wang, L. Su, S. Jiang, B. Wang, B. Y. M. Ip, H. Ko, T. W. H. Leung, P. W. Y. Chiu, S. C. H. Yu, L. Zhang, Tracking and navigation of a microswarm under laser speckle contrast imaging for targeted delivery. *Sci. Robot.* **9**, eadh1978 (2024).
24. Y. Alapan, U. Bozuyuk, P. Erkoc, A. C. Karacakol, M. Sitti, Multifunctional surface microrollers for targeted cargo delivery in physiological blood flow. *Sci. Robot.* **5**, eaba5726 (2020).
25. V. Garcia-Gradilla, J. Orozco, S. Sattayasamitsathit, F. Soto, F. Kuralay, A. Pourazary, A. Katzenberg, W. Gao, Y. F. Shen, J. Wang, Functionalized ultrasound-propelled magnetically guided nanomotors: Toward practical biomedical applications. *ACS Nano* **7**, 9232–9240 (2013).
26. A. Del Campo Fonseca, C. Glück, J. Droux, Y. Ferry, C. Frei, S. Wegener, B. Weber, M. El Amki, D. Ahmed, Ultrasound trapping and navigation of microrobots in the mouse brain vasculature. *Nat. Commun.* **14**, 5889 (2023).
27. M. Kaynak, A. Ozcelik, A. Nourhani, P. E. Lammert, V. H. Crespi, T. J. Huang, Acoustic actuation of bioinspired microswimmers. *Lab Chip* **17**, 395–400 (2017).
28. D. Ahmed, T. Baasch, B. Jang, S. Pane, J. Dual, B. J. Nelson, Artificial swimmers propelled by acoustically activated flagella. *Nano Lett.* **16**, 4968–4974 (2016).
29. Y. Deng, A. Paskert, Z. Zhang, R. Wittkowski, D. Ahmed, An acoustically controlled helical microrobot. *Sci. Adv.* **9**, eadh5260 (2023).
30. W. Wang, L. A. Castro, M. Hoyos, T. E. Mallouk, Autonomous motion of metallic microrods propelled by ultrasound. *ACS Nano* **6**, 6122–6132 (2012).
31. W. Wang, S. Li, L. Mair, S. Ahmed, T. J. Huang, T. E. Mallouk, Acoustic propulsion of nanorod motors inside living cells. *Angew. Chem. Int. Ed.* **53**, 3201–3204 (2014).
32. J. Rufo, F. Cai, J. Friend, M. Wiklund, T. J. Huang, Acoustofluidics for biomedical applications. *Nat. Rev. Methods Primers* **2**, 30 (2022).
33. J. Rufo, P. Zhang, R. Zhong, L. P. Lee, T. J. Huang, A sound approach to advancing healthcare systems: The future of biomedical acoustics. *Nat. Commun.* **13**, 3459 (2022).
34. A. Del Campo Fonseca, T. Kohler, D. Ahmed, Ultrasound-controlled swarmbots under physiological flow conditions. *Adv. Mater. Inter.* **9**, 2200877 (2022).
35. C. Dillinger, J. Knipper, N. Nama, D. Ahmed, Steerable acoustically powered starfish-inspired microrobot. *Nanoscale* **16**, 1125–1134 (2024).
36. D. Ahmed, T. Baasch, N. Blondel, N. Läubli, J. Dual, B. J. Nelson, Neutrophil-inspired propulsion in a combined acoustic and magnetic field. *Nat. Commun.* **8**, 770 (2017).
37. D. Ahmed, A. Sukhov, D. Hauri, D. Rodrigue, G. Maranta, J. Harting, B. J. Nelson, Bioinspired acousto-magnetic microswarm robots with upstream motility. *Nat. Mach. Intell.* **3**, 116–124 (2021).
38. Z. Zhang, A. Sukhov, J. Harting, P. Malgaretti, D. Ahmed, Rolling microswarms along acoustic virtual walls. *Nat. Commun.* **13**, 7347 (2022).
39. L. Ren, N. Nama, J. M. McNeill, F. Soto, Z. Yan, W. Liu, W. Wang, J. Wang, T. E. Mallouk, 3D steerable, acoustically powered microswimmers for single-particle manipulation. *Sci. Adv.* **5**, eaax3084 (2019).
40. A. Aghakhani, O. Yasa, P. Wrede, M. Sitti, Acoustically powered surface-slipping mobile microrobots. *Proc. Natl. Acad. Sci. U.S.A.* **117**, 3469–3477 (2020).
41. A. Aghakhani, A. Pena-Francesch, U. Bozuyuk, H. Cetin, P. Wrede, M. Sitti, High shear rate propulsion of acoustic microrobots in complex biological fluids. *Sci. Adv.* **8**, eabm5126 (2022).
42. A. Del Campo Fonseca, D. Ahmed, Ultrasound robotics for precision therapy. *Adv. Drug Deliv. Rev.* **205**, 115164 (2024).
43. S. Mohanty, Y.-H. Lin, A. Paul, M. R. P. Van Den Broek, T. Segers, S. Misra, Acoustically actuated flow in microrobots powered by axisymmetric resonant bubbles. *Adv. Intell. Syst.* **6**, 2300465 (2024).
44. M. Kaynak, P. Dirix, M. S. Sakar, Addressable acoustic actuation of 3D printed soft robotic microsystems. *Adv. Sci.* **7**, 2001120 (2020).
45. S. Hilgenfeldt, D. Lohse, M. Zomack, Response of bubbles to diagnostic ultrasound: A unifying theoretical approach. *Eur. Phys. J. B* **4**, 247–255 (1998).
46. M. Versluis, E. Stride, G. Lajoinie, B. Dollet, T. Segers, Ultrasound contrast agent modeling: A review. *Ultrasound Med. Bio.* **46**, 2117–2144 (2020).
47. L. A. Crum, Bjerknes forces on bubbles in a stationary sound field. *J. Acoust. Soc. Am.* **57**, 1363–1370 (1975).
48. J. M. McNeill, N. Nama, J. M. Braxton, T. E. Mallouk, Wafer-scale fabrication of micro- to nanoscale bubble swimmers and their fast autonomous propulsion by ultrasound. *ACS Nano* **14**, 7520–7528 (2020).
49. D. Ahmed, C. Dillinger, A. Hong, B. J. Nelson, Artificial acousto-magnetic soft microswimmers. *Adv. Mater. Technol.* **2**, 1700050 (2017).
50. M. B. Browning, S. N. Cereceres, P. T. Luong, E. M. Cosgriff-Hernandez, Determination of the in vivo degradation mechanism of PEGDA hydrogels: In vivo degradation mechanism of PEGDAA. *J. Biomed. Mater. Res. A* **102**, 4244–4251 (2014).

51. H. Lee, D.-I. Kim, S.-H. Kwon, S. Park, Magnetically actuated drug delivery helical microrobot with magnetic nanoparticle retrieval ability. *ACS Appl. Mater. Interfaces* **13**, 19633–19647 (2021).
52. J. Park, C. Jin, S. Lee, J.-Y. Kim, H. Choi, Magnetically actuated degradable microrobots for actively controlled drug release and hyperthermia therapy. *Adv. Healthc. Mater.* **8**, 1900213 (2019).
53. R. Legay, S. Massou, J. Azéma, R. Martino, M. Malet-Martino, Hydrolytic pathway of 5-fluorouracil in aqueous solutions for clinical use. *J. Pharm. Biomed. Anal.* **98**, 446–462 (2014).
54. R. B. Diasio, B. E. Harris, Clinical pharmacology of 5-fluorouracil. *Clin. Pharmacokinet.* **16**, 215–237 (1989).
55. T. Gwisai, N. Mirkhani, M. G. Christiansen, T. T. Nguyen, V. Ling, S. Schuerle, Magnetic torque–driven living microrobots for increased tumor infiltration. *Sci. Robot.* **7**, eabo0665 (2022).
56. A. C. Hortelão, R. Carrascosa, N. Murillo-Cremaes, T. Patiño, S. Sánchez, Targeting 3D bladder cancer spheroids with urease-powered nanomotors. *ACS Nano* **13**, 429–439 (2019).
57. Z. Cong, S. Tang, L. Xie, M. Yang, Y. Li, D. Lu, J. Li, Q. Yang, Q. Chen, Z. Zhang, X. Zhang, S. Wu, Magnetic-powered Janus cell robots loaded with oncolytic adenovirus for active and targeted virotherapy of bladder cancer. *Adv. Mater.* **34**, 2201042 (2022).
58. A. Arbabian, T. C. Chang, M. L. Wang, J. Charthad, S. Baltsavias, M. Fallahpour, M. J. Weber, Sound technologies, sound bodies: Medical implants with ultrasonic links. *IEEE Microw. Mag.* **17**, 39–54 (2016).
59. P. M. Morse, K. U. Ingard, *Theoretical Acoustics* (Princeton Univ. Press, 1986).
60. A. D. Pierce, *Acoustics: An Introduction to Its Physical Principles and Applications* (Springer, 2019).
61. P. B. Muller, R. Barnkob, M. J. H. Jensen, H. Bruus, A numerical study of microparticle acoustophoresis driven by acoustic radiation forces and streaming-induced drag forces. *Lab Chip* **12**, 4617–4627 (2012).
62. W. L. Nyborg, Acoustic streaming due to attenuated plane waves. *J. Acoust. Soc. Am.* **25**, 68–75 (1953).
63. A. Dolev, M. Kaynak, M. S. Sakar, Dynamics of entrapped microbubbles with multiple openings. *Phys. Fluids* **34**, 012012 (2022).
64. N. Bertin, T. A. Spelman, O. Stephan, L. Gredy, M. Bouriau, E. Lauga, P. Marmottant, Propulsion of bubble-based acoustic microswimmers. *Phys. Rev. Appl.* **4**, 064012 (2015).
65. Y. Sun, X. Wang, J. Yu, Eds., *Field-Driven Micro and Nanorobots for Biology and Medicine* (Springer International Publishing, 2022).

Acknowledgments: We acknowledge critical support and infrastructure provided for this work by the Kavli Nanoscience Institute at Caltech. We thank H. Li and Y. Yao for valuable inputs, D. M. Silevitch for support in characterizing the magnetic properties of BAMs, and A. Dolev for useful discussions on numerical simulations. We also acknowledge Port Therapeutics for providing access to the IVIS. Figures 2O, 3H, 4A, 4H, 4J, 4L, and 5A were created with BioRender. **Funding:** This work was supported by National Science Foundation [grant 1931214 (to W.G.) and grants 1931292 and 2323046 (to O.S.P.)]; Heritage Medical Research Institute (to W.G.); Singapore Ministry of Education Academic Research Fund [MOE-T2EP50221-0012 (to L.Z.)]; National Institutes of Health grants R01EY030126, R01EY032229, and R01EY035084 (to Q.Z.); Army Research Office through Institute for Collaborative Biotechnologies (to J.R.G.); Caltech DeepMIC Center, with the support of the Caltech Beckman Institute and the Arnold and Mabel Beckman Foundation (to D.W. and M.G.S.); and David and Lucile Packard Foundation (to M.G.S.). **Author contributions:** Conceptualization: W.G. and H.H. Methodology: H.H., X.M., W.D., J.Z., and S.T. Investigation: H.H., X.M., W.D., J.Z., S.T., O.S.P., L.Z., E.C.-H., C.G., E.K., J.Y., M.Y., A.L., C.W, H.K.S., P.N.P, C.L.H., P.J.G., L.L., Y.Z., J.O.D., L.V.W., M.G.S., and D.W. Visualization: H.H., X.M., J.Z., D.W., L.L., and Y.Z. Funding acquisition: W.G., O.S.P., M.G.S., Q.Z., and J.R.G. Project administration: W.G. Supervision: W.G., D.W., Q.Z., and J.R.G. Writing—original draft: W.G., H.H., and X.M. Writing—review and editing: H.H., X.M., W.D., J.Z., S.T., O.S.P., L.Z., E.C.-H., C.G., E.K., J.Y., M.Y., A.L., C.W, H.K.S., P.N.P., C.L.H., P.J.G., L.L., Y.Z., J.O.D., L.V.W., M.G.S., D.W., Q.Z., J.R.G., and W.G. **Competing interests:** The authors declare that they have no competing interests. **Data and materials availability:** All data needed to support the conclusions of this manuscript are included in the main text or Supplementary Materials.

Submitted 21 March 2024
Accepted 11 November 2024
Published 11 December 2024
10.1126/scirobotics.adp3593